Planetary and Space Science 96 (2014) 51–61

Contents lists available at ScienceDirect

Planetary and Space Science

journal homepage: www.elsevier.com/locate/pss

Olivine alteration and H_2 production in carbonate-rich, low temperature aqueous environments

Anna Neubeck [a,*], Nguyen Thanh Duc [b], Helge Hellevang [c], Christopher Oze [d], David Bastviken [e], Zoltán Bacsik [f], Nils G. Holm [a]

[a] Department of Geological Sciences, Stockholm University, Sweden
[b] Earth Systems Research Center, University of New Hampshire, USA
[c] Department of Environmental Geology and Hydrology, University of Oslo, Norway
[d] Department of Geological Sciences, University of Canterbury, New Zealand
[e] Department of Thematic Studies – Water and Environmental Studies, Linköping University, Sweden
[f] Department of Materials and Environmental Chemistry, Stockholm University, Sweden

ARTICLE INFO

Article history:
Received 26 June 2013
Received in revised form
25 February 2014
Accepted 26 February 2014
Available online 22 March 2014

Keywords:
Olivine
Hydrogen
Serpentinization
Deep biosphere
Early Earth
Habitability

ABSTRACT

Hydrous alteration of olivine is capable of producing molecular hydrogen (H_2) under a wide variety of hydrothermal conditions. Although olivine hydrolysis (i.e., serpentinization) has commonly been assessed at elevated temperatures (> 100 °C), the nature of these reactions in relation to H_2 production at lower temperatures has not been systematically evaluated, especially with regard to carbonate-rich fluids. Specifically, carbonate formation may kinetically infringe on geochemical routes related to serpentinization and H_2 production at lower temperatures. Here time-dependent interactions of solid, liquid, and gaseous phases with respect to olivine hydrolysis in a carbonate-rich solution (20 mM HCO_3^-) at 30, 50 and 70 °C for 315 days is investigated experimentally. Within the first two months, amorphous Si-rich (i.e., talc-like) and carbonate phases precipitated; however, no inhibition of olivine dissolution is observed at any temperature based on surface chemistry analyses. High-resolution surface analyses confirm that precipitates grew as spheroids or vertically to form topographic highs allowing further dissolution of the free olivine surfaces and exposing potential catalysts. Despite no magnetite (Fe_3O_4) being detected, H_2 increased with time in experiments carried out at 70 °C, indicating an alternative coupled route for Fe oxidation and H_2 production. Spectrophotometry analyses show that aqueous Fe(II) is largely converted to Fe(III) potentially integrating into other phases such as serpentine and talc, thus providing a viable pathway for H_2 production. No increase in H_2 production was observed in experiments carried out at 30 and 50 °C supporting observations that incorporation of Fe(II) into carbonates occurred faster than the intertwined processes of olivine hydrolysis and Fe(III) oxidation. Overall, carbonate formation is confirmed to be a major influence related to H_2 production in low-temperature serpentinization systems.

1. Introduction

Ultramafic rocks comprise a major part of the oceanic lithosphere and consist of up to 50% of olivine (McDonough and Sun, 1995; Sobolev et al., 2005). Some olivine-rich systems on Earth are present within habitable, low-temperature aqueous environments and are undergoing hydrolysis (i.e., serpentinization, from Oze et al. (2012)). Hydrolysis of olivine can result in the formation of molecular hydrogen (H_2) as a result of the oxidation of ferrous iron (Fe(II)) in olivine and the concomitant reduction of water as shown below.

$$(Mg_{0.88}Fe_{0.12})_2SiO_4 + 1.34H_2O \rightarrow \text{olivine} + \text{water}$$

$$0.5Mg_3Si_2O_5(OH)_4 + 0.26Mg(OH)_2 + 0.08Fe_3O_4 + 0.08H_2$$

$$\text{serpentine} + \text{brucite} + \text{magnetite} + \text{dihydrogen} \quad (1)$$

Usually, ferric iron (Fe(III)) is incorporated into magnetite (Fe_3O_4), brucite ($Mg(OH)_2$) and/or serpentine minerals ($(Mg,Fe)_3Si_2O_5(OH)_4$) depending on activity of Si, water to rock ratios, temperature and compositional differences of the protolith; however, not all reactions lead to the formation of H_2 (Evans, 2008; Frost and Beard, 2007; Klein et al., 2013; McCollom and Bach, 2009; Seyfried et al., 2007). When H_2 is formed it serves as a strong reducing agent in many reactions, thus contributing to the presence of reduced species within the

* Corresponding author at: Svante Arrhenius väg 8, SE-10691 Stockholm, Sweden. Tel.: +46 73 73148 84.
E-mail addresses: anna.neubeck@geo.su.se (A. Neubeck), nguyen.duc@geo.sr.se (N.T. Duc), helge.hellevang@geo.uio.no (H. Hellevang), christopher.oze@canterbury.ac.nz (C. Oze), david.bastviken@liu.se (D. Bastviken), zoltan.bacsik@mmk.su.se (Z. Bacsik), nils.holm@geo.su.se (N.G. Holm).

http://dx.doi.org/10.1016/j.pss.2014.02.014

serpentinization system such as Ni–Fe-alloys, CH_4, magnetite and hydrocarbons (Berndt et al., 1996; Charlou et al., 2002; Frost, 1985; Frost and Beard, 2007; Haggerty, 1991; Holm and Charlou, 2001; Konn et al., 2009). In basaltic environments in which the Si concentration is higher, the serpentinization reaction commonly leads to the formation of talc and serpentine (Hietanen, 1973).

$$3(Mg,Fe)_2SiO_4 + 5SiO_2 + 2H_2O \rightarrow 2(Mg,Fe)_3(OH)_2Si_4O_{10} \quad (2)$$

Molecular hydrogen (H_2) is an essential metabolic component for many microbial species, indicating that serpentine systems, such as oceanic peridotites, continental basalts and peridotite-hosted hydrothermal systems, could be suitable for hosting microbes (Evans, 2008; Frost and Beard, 2007; Früh-Green et al., 2004; Hellevang, 2008; Klein et al., 2013; Krumholz, 2000; McCollom and Bach, 2009; Nealson et al., 2005; Pedersen, 1993; Schulte et al., 2006; Schwarzenbach et al., 2013; Seyfried et al., 2007; Sleep et al., 2011). Even though H_2 formation rate is slow at low temperatures needed for microbial life (< 110 °C), it has been shown that some methanogenic archaea have the possibility to grow at very low H_2 pressures (Berndt et al., 1996; Charlou et al., 2002; Frost, 1985; Frost and Beard, 2007; Haggerty, 1991; Holm and Charlou, 2001; Konn et al., 2009; Kral et al., 1998; Schnürer et al., 1997), which is consistent with the findings in natural systems. This means that as long as the concentration of H_2 formed is equal to the microbial need, it will support the growth of the microbial community. However, the survival of a microbial community can be sustained with even lower H_2 levels as some species can be dormant and wait for higher H_2 concentration to accumulate (Hugoni et al., 2013). In Si-rich, basaltic systems, there is usually enough H_2 for sustaining some microbial communities (Sleep et al., 2011).

In some of the low temperature environments mentioned above, carbonates are common and may influence the hydrolysis of olivine (Giammar et al., 2005; Hänchen et al., 2008; 2006; Pokrovsky and Schott, 2000a; 2000b; Prigiobbe et al., 2009). Some studies report a dissolution rate decrease of olivine in a solution with added HCO_3^- (Pokrovsky and Schott, 2000a), whereas others show an olivine dissolution rate not affected by the addition of HCO_3^- (Golubev et al., 2005). In any case, low-reactive carbonates and hydroxides may precipitate and cover the surface of the dissolving olivine, thus preventing further access to the solution and the coupled dissolution (Golubev et al., 2005). Also, ferrous iron has been shown to be incorporated into carbonates more rapidly than the oxidation into ferric iron, which will concomitantly prevent the formation of H_2 and CH_4 (Jones et al., 2010). Notably, it was also shown that the precipitation of carbonates only temporarily decreased the production of H_2, but the production increased again after the removal of excess carbonates due to precipitation. In the case of a continuous supply of HCO_3^- species in a solution, H_2 and CH_4 formation will be at a minimum. Additionally, the presence of Si in the solution may lead to the co-precipitation of silica and carbonates, which will stabilize the amorphous carbonate species and prevent any further chemical exchange with the solution (Kellermeier et al., 2010). This should result in a decrease of olivine dissolution due to the insoluble silica and carbonate products on the surface.

In this study we investigate the potential abiotic formation of H_2 through the experimental alteration of olivine in habitable environments rich in Na-carbonate and with an increasing concentration of Si. The objective is to evaluate the ability of forming H_2 through the experimental low temperature alteration of olivine in the presence of HCO_3^- and Si and to investigate the possibility of accumulating enough H_2 for microbial growth according to earlier studies (Kral et al., 1998; Schnürer et al., 1997). Low temperature serpentinization experiments in an environment with Si and HCO_3^- may clarify pathways for H_2 formation even at temperatures too low to produce magnetite.

2. Materials and methods

All details of the experimental, modeling and analytical methods are presented in Appendix A as supplementary information. Below is a brief summary of the experimental setup. Olivine sand (specific surface area of 0.4044 m^2/g) was exposed to an aqueous 20 mM Na-carbonate (Na_2CO_3) solution at 30 °C, 50 °C and 70 °C and with increasing Si concentrations (0.3–0.9 mM at 30 °C, 0.4–0.9 mM at 50 °C and 0.4–3.8 mM at 70 °C) to investigate the influence of temperature, Si concentration and HCO_3^- on the formation of carbonates and the formation of H_2.

The geochemical software PHREEQC-2 (Parkhurst and Appleo, 1999) was used to simulate the kinetic olivine alteration and formation of secondary mineral phases. We utilized the llnl.dat database based on the thermo.com.V8.R6.230 thermodynamic dataset prepared at the Lawrence Livermore National Laboratory. We first estimated the thermodynamic stability of forsterite90 by defining an ideal solid-solution between two end-members forsterite (pure Mg-olivine) and fayalite (Fe-endmember). This Fo90 composition is similar to the ones used in the present experimental study and also in experiments used to derive rate constants for the kinetic simulations (Pokrovsky and Schott, 2000a; Oelkers et al., 2008). We then used the estimated Fo90 equilibrium constant and temperature dependence in the following simulations. The forsterite was defined to dissolve according to the rate equations given in Appendix A2. Secondary phases were allowed to form as soon as they reached supersaturation. From mineral phases in the llnl.dat database, we chose talc, hematite, magnetite, quartz, siderite, goethite and brucite as possible secondary phases. To track the gas evolution in PHREEQC we used the GAS_PHASE keyword, allowing a constant-volume simulation for the gas phase equilibrated with the aqueous solution.

3. Results and discussions

3.1. Liquid phase

All raw ICP data can be found in Appendix A. The concentration (ppb) of Zn in solution increases linearly with time and temperature (Fig. 1a–c), which makes Zn a suitable tracer for olivine alteration. Using Zn as a tracer gives a calculated average net dissolution rate (sample-blanks) of 1.55 nmol/day at 30 °C, 3.07 nmol/day at 50 °C and 13.50 nmol/day at 70 °C. All rates calculated from Zn are released into solution. The Zn concentration in the olivine bulk material was 48.8 ppm (Appendix A, (Haug et al., 2010)). By using the dissolution rates calculated from Zn release, the calculated Fe concentration in solution is sufficient to form all the measured H_2 (average rate of 0.51 nmol/day) in the headspace.

In contrast to the Zn concentrations, Mg and Fe fluctuate at 30 °C (Fig. 1d and g). There is an initial increase in the concentrations of Mg and Fe, which likely reflects enhanced dissolution of the two elements during autoclaving. At higher temperatures, Mg and Fe concentrations decrease and stabilize (Fig. 1e,f and h,i). At 70 °C, the Mg and Fe concentrations decrease rapidly to almost zero after 133 days and seem to reach a steady-state (Fig. 1f and i). The decrease of elements in solution can be explained by precipitation on the surface of the olivine and within the liquid, see Section 3.2. The total concentration (ppb) of Si increases with both time and temperature (Fig. 1j–l). The average net Si concentrations fluctuate within the limits of error when the blank Si input is subtracted from the samples (sample-blank, nmol, Fig. 1m–o) resulting in Si rates of 4.99 mmol/day at 30 °C, 2.69 mmol/day at 50 °C and 0.81 mmol/day at 30 °C. This shows that Si is precipitating at a rate that increases with increasing temperature, which is consistent with the observations that the precipitates

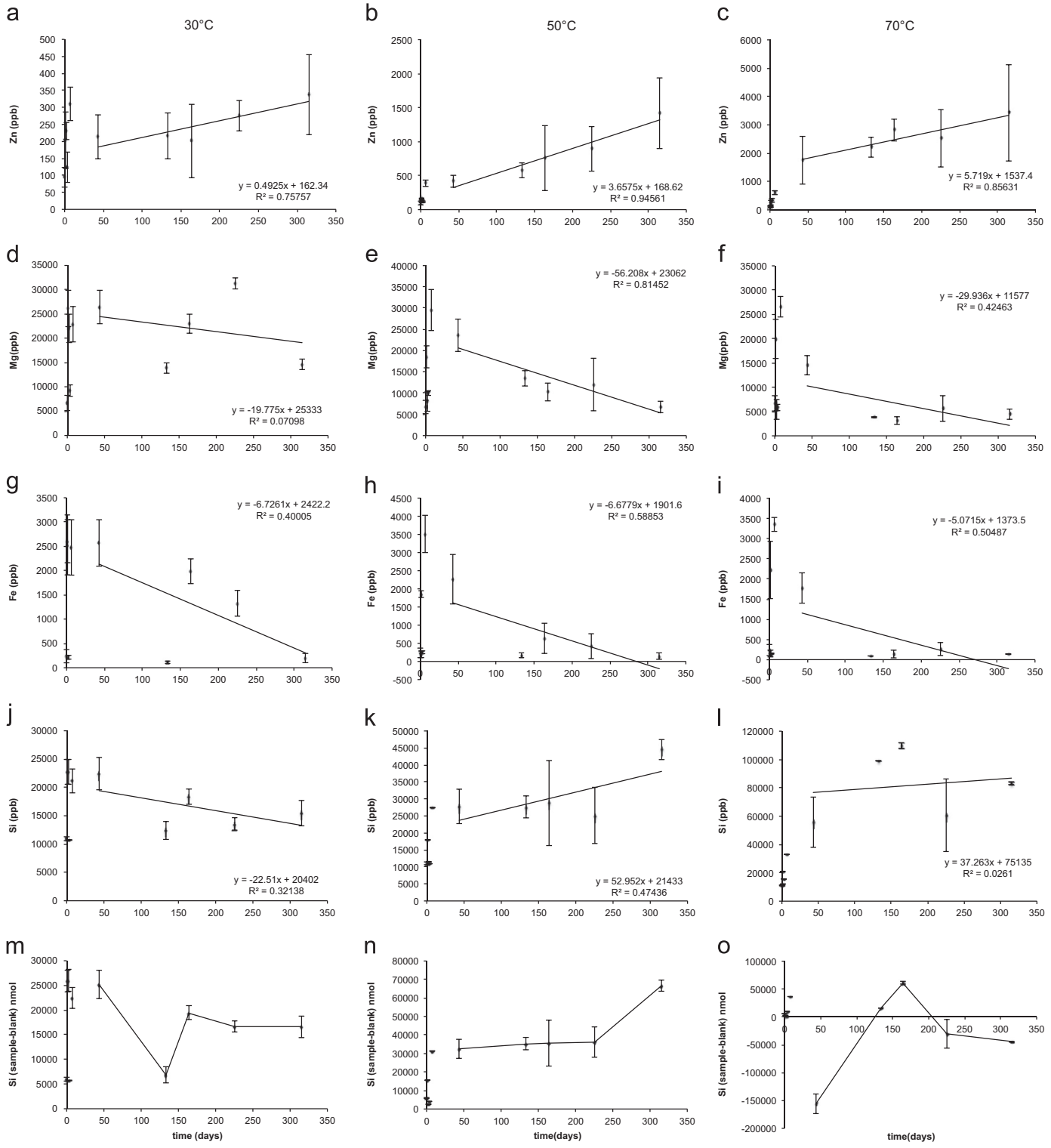

Fig. 1. Measured (with ICP-AES) concentrations of Zn (a–c, ppb), Mg (d–f, ppb), Fe (g–i, ppb), Si (j–l, ppb) and Si (m–o, nmol) in solution in the experiments carried out at 30 (a, d, g, j, m), 50 (b, e, h, k, n) and 70 °C (c, f, i, l, o) experiments. Featured plots show the total amount of the element concentration in ppb. No withdrawal of control input was made. The error bars reflect the differences in sample conditions and not measurement errors. The Si concentrations showed in (m–o) show the net concentration of Si in solution in nmol where blank samples have been withdrawn from the samples.

were mainly found in samples of experiments carried out at 70 °C; see Section 3.2.

Some liquid samples were analyzed for Fe(II) and Fe(III) using spectrophotometry. The absorbance for Fe(II) was an order of magnitude less than the lowest standard curve measurement. This means that a quantitative estimation of the Fe(II) concentration could not be established. It can, however, be concluded that the total amount of Fe(II) in the samples was less than 0.025 ppm and that the residual Fe was Fe(III) at all temperatures and after 315 days of incubation. The total Fe concentration measured by ICP-OES in the bottles was higher than the estimated concentrations of Fe(II) and Fe(III) due to the filtration of colloidal Fe species that

made the solutions slightly cloudy. The total Fe in solution could not be quantified; however, the increase in absorbance confirms the presence of Fe(III).

3.2. Solid phase

All olivine bulk data is represented in Appendix A. Mineralogical analyses of the initial olivine material using XRD and Raman show that the sample is 96% forsterite-dominated olivine ($Mg_{1.8}Fe_{0.2}SiO_4$) with 4% accessory minerals such as clinochlore ($(Mg_5Al)(AlSi_3)O_{10}(OH)_8$), phlogopite ($KMg_3AlSi_3O_{10}(F,OH)_2$), talc ($Mg_3Si_4O_{10}(OH)_2$) and small amounts (less than 1%) of Cr- and Fe-bearing magnetite/spinel (Neubeck et al., 2011). Traces of hornblende and mica have also been observed by Haug et al. (2010). Magnesite ($MgCO_3$) is present in all XRD spectra but barely over noise level. Final (after experiment termination) XRD analyses of material incubated for 315 days show some lowering of the initial peaks but the differences are small.

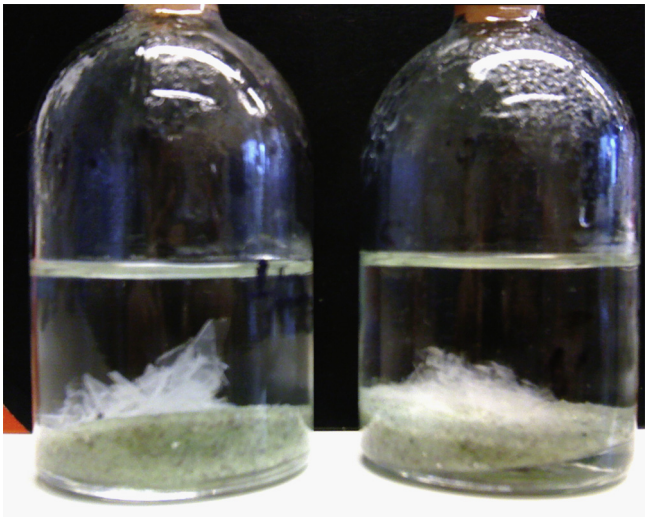

Fig. 2. Incubation bottles and precipitates as white sheets floating in the solution in experiments carried out at 70 °C.

After less than 43 days of incubation, white, sheet-like precipitates started to form in bottles used when carrying out the experiment at 70 °C (Fig. 2). When washed with 95% ethanol and Milli-Q water, dried and analyzed by ESEM, four different phases (Fig. 3) are present: 1) a sheet-like Si, Mg and C-rich phase (Fig. 3a), 2) an Fe-containing phase also coupled with sheet-like phases (Fig. 3b), 3) a phase consisting of 1–2 μm spheres of Mg, C and Si (Fig. 3c) and 4) a phase consisting of small ≈1 μm sized spheres consisting of Zn, S, Mg, Si and C (Fig. 3d) always incorporated into the sheet-like precipitate. When treated with acid, parts of the precipitate dissociated in a strong bubbling reaction from CO_2 escape. The residual precipitate is strongly attached to the glass slide and consists of Mg- and Si-bearing crystals. The sheet-like and Fe-containing phases have Mg/Si ratios around 0.82 and 0.92 respectively, and these ratios are between serpentine (1.5) and talc (0.75). Chrysotile was detected with Raman spectroscopy but not with XRD, which could be due to incomplete formation of well-defined crystals such as the formation of microcrystalline/amorphous talc-like secondary phases. No precipitates could be observed in the 30 °C and 50 °C experiments. Hydrated

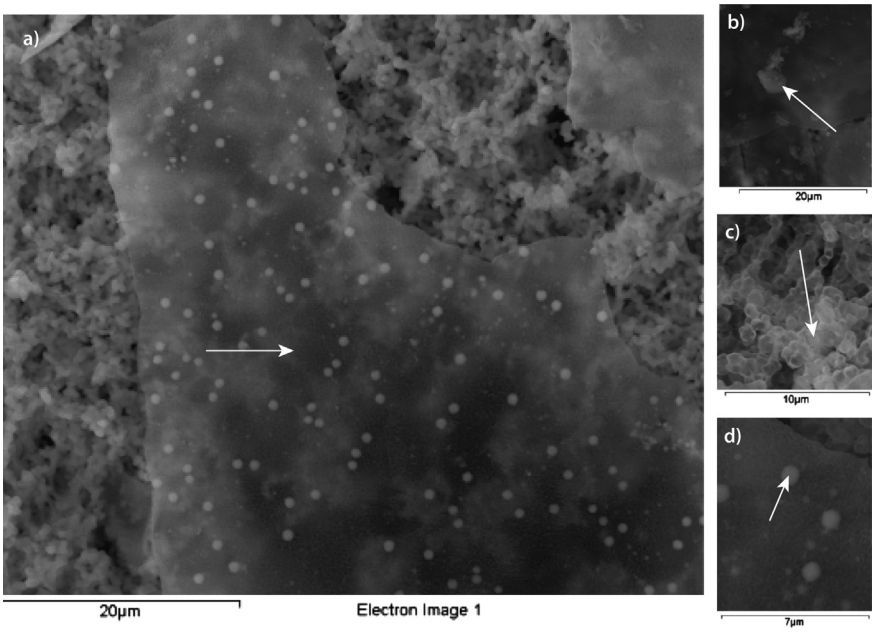

	a	b	c	d
Element	wt%	wt%	wt%	wt%
C	2.37	18.76	23.84	22.05
Mg	1.94	18.04	2.95	2.85
Si	2.38	19.56	3.62	2.49
O	71.07	49.96	69.59	66.5
S				2.05
Zn				5.73
Fe		7.43		

Fig. 3. ESEM-EDS images of the precipitates forming in the bottles at 70 °C, where (a) shows the sheet-like precipitates, (b) an Fe-rich amorphous phase, (c) carbonate-rich spheres and (d) Zn-containing spheres. The arrows point out from where the EDS-spectra were taken.

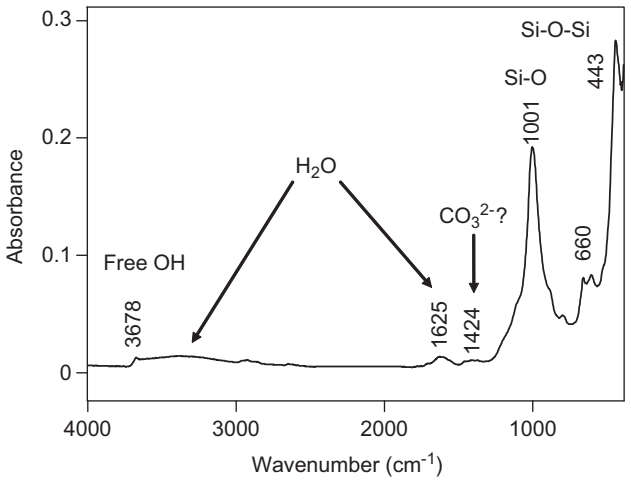

Fig. 4. Infrared spectrum of the filtered and washed precipitate where the band at 3678 cm^{-1} belongs to free OH-groups. H_2O is represented in OH stretching bands between 3490–3280 cm^{-1} and the band at 1625 cm^{-1}. The bands at 1001, 660 and 443 cm^{-1} belong to Si–O(–Si) asymmetric stretching, symmetric stretching and bending modes respectively. The band at 1424 cm^{-1} indicates the presence of carbonates in the sample.

magnesium silicates with talc-resembling structures were detected by IR (with a spectral resolution of 4 cm^{-1}) and traces of carbonates could not be excluded (Fig. 4). The material is silicate. From reference library of IR spectra (Sadtler IR database of inorganic materials) hydrated magnesium silicate shows the best match. Bands for isolated OH group (can be MgOH) and OH groups in structural or physisorbed water can be observed and is represented by stretching band at 3678 cm^{-1}. The broad band at 1424 cm^{-1} may belong to carbonate ions. A splitting in the sharp bands of isolated OH groups is present. This splitting is typical in talc-like compounds when other divalent cations replace Mg^{2+} ions (Wilkins and Ito, 1967). The extent of this replacement may not be very significant as the split of Si–O bands (stretching band at 1001 cm^{-1} and the Si–O–Si deformation band at 443 cm^{-1}) is not observed in contrast to IR spectra of similar structures (Golightly and Arancibia, 1979; Wilkins and Ito, 1967; Yariv and Heller-Kallai, 1975).

Precipitated secondary minerals on the olivine surface were analyzed with ESEM and showed the presence of small Fe-containing crystals with a molar ratio close to serpentine. Also Mg/Si ratio was 1.6, which is close to serpentine. The difference between the precipitates in solution and on the surface is the amount of Mg compared with Si. The concentration of Mg is higher in precipitates on the olivine surface compared with precipitates in solution, suggesting a transition from olivine (Mg/Si=2) through serpentine (Mg/Si=1.5) and forward to talc (Mg/Si=0.75).

About 1% of the Fe(II) in the incubated olivine is shown to be converted to Fe(III) using Mössbauer spectroscopy. In contrast, about 8% of the precipitates within the solution was measured to be Fe(III), even though the data may not truly reflect Fe oxidation process due to the possibility that some of the Fe(II) within the precipitate was oxidized during the drying process. No peaks coincided with magnetite or hematite. Magnetite is reported to be unstable at temperatures less than 150 °C (Klein et al., 2013) which could explain the lack of observed magnetite as well as slow kinetics at prevailing experimental temperatures. Also, a system with high Si activity favors the uptake of Fe into talc prior to magnetite (Frost and Beard, 2007; Mayhew et al., 2013).

Surface, single-grain spot analyses with XPS show a decrease in Fe, a shift in the Mg line, an increase and shift in Si as well as the appearance of a carbonate line (line 290.1) on the weathered grain surface (Fig. 5). Shift in Si 2p peaks to a higher binding energy is consistent with the formation of silica and shift in Mg 2s peaks to a higher binding energy is consistent with oxidation of Mg (Schulze et al., 2004). This suggests formation of talc/serpentine and carbonates in the bottles and on the olivine surface.

A reduction in topographical scaling by 8.99% but increased roughness of the surface is observed with profilometry (compare legends in Fig. 6a and b). This means that differences between the highest and the lowest points on the olivine surface are less on the incubated olivine surface in comparison to the initial surface. However, the roughness of the surface on a smaller scale has increased on the incubated olivine surface in comparison to the initial olivine surface. Initial pits are partly filled with precipitates and the topographic differences decrease. Small, rounded structures with sizes of 2 μm or less are present on the surface after nearly one year of incubation (Fig. 6b). These rounded crystals were measured with XPS (Fig. 5) and the binding energy (1022.9 eV) for the Zn line coincided with ZnO (Khallaf et al., 2009) or possibly ZnS (Xu et al., 1998).

Due to this experimental system being far from equilibrium and the inherent slow reaction rates, the talc/serpentine resembling phase is probably a metastable, poorly crystalline, intermediate serpentine and/or talc phase.

3.3. H_2 gas

A rapid increase in H_2 generation to a maximum of 11.25 ± 0.30 nmol/g olivine was observed (Fig. 7) at the beginning of the experiment and is interpreted to be caused by autoclaving of bottles together with the olivine. An increase from 2.65 ± 0.44 to 3.79 ± 0.35 nmol/g of olivine was observed in experiments carried out at 70 °C between days 43 and 315 (Fig. 7c) whereas the H_2 concentration in experiments carried out at 30 and 50 °C was stable around 3.12 ± 0.39 and 3.48 ± 0.31 respectively (Fig. 7a and b). A slope–intercept trendline for the data between day 43 to 315 increases the rate of H_2 formation by 0.0001 at 30 °C, 0.0004 at 50 °C and 0.0042 at 70 °C.

The use of control samples shows that the background H_2 was too low to explain the accumulated H_2 in experiments. Also, no hydrocarbons were distinguishable with IR within the material, neither in the pure olivine nor in accessory minerals. No gas phases were observed in any of the spinel melt inclusions found in the material and no significant CH_4 or adsorbed H_2 amounts were observed within the unweathered olivine crystals. Little or no OH groups are present within the pure olivine crystals, whereas intense OH bands are observed within the accessory minerals (Fig. 8). This means that the accessory minerals may contain adsorbed water and/or OH groups in a larger amount than in the pure olivine crystals. The intensity variation of the OH groups in both plots (Fig. 8 a and b) may depend on the orientation of the olivine crystals but some of the observed H_2 may have been released from accessory minerals present in the initial bulk material. Oxidation of Fe(II) through olivine and accessory mineral alteration is another possible source of H_2. According to Mayhew et al. (2013) spinels play an important role in the generation of H_2 both through the direct reduction of water at the mineral surface and/or by the interfacial electron transfer between the spinel surface and the adsorbed aqueous Fe(II). This is a possible source in this experiment because of the presence of accessory spinels. However, the bulk material surface measurements using XPS before and after incubation show an almost total disappearance of Fe from the surface (Fig. 5). This suggests that other phases could host Fe(II) for H_2 generation as well. Fe(III) could be incorporated into talc and serpentine (see the simplified Eq. (3)) which could contribute to the generation of H_2 (Evans, 2010; Forbes, 1969, 1971; Klein et al., 2013; Marcaillou et al., 2011; Noack et al., 1986). Forbes (1969) describes that low temperature talc

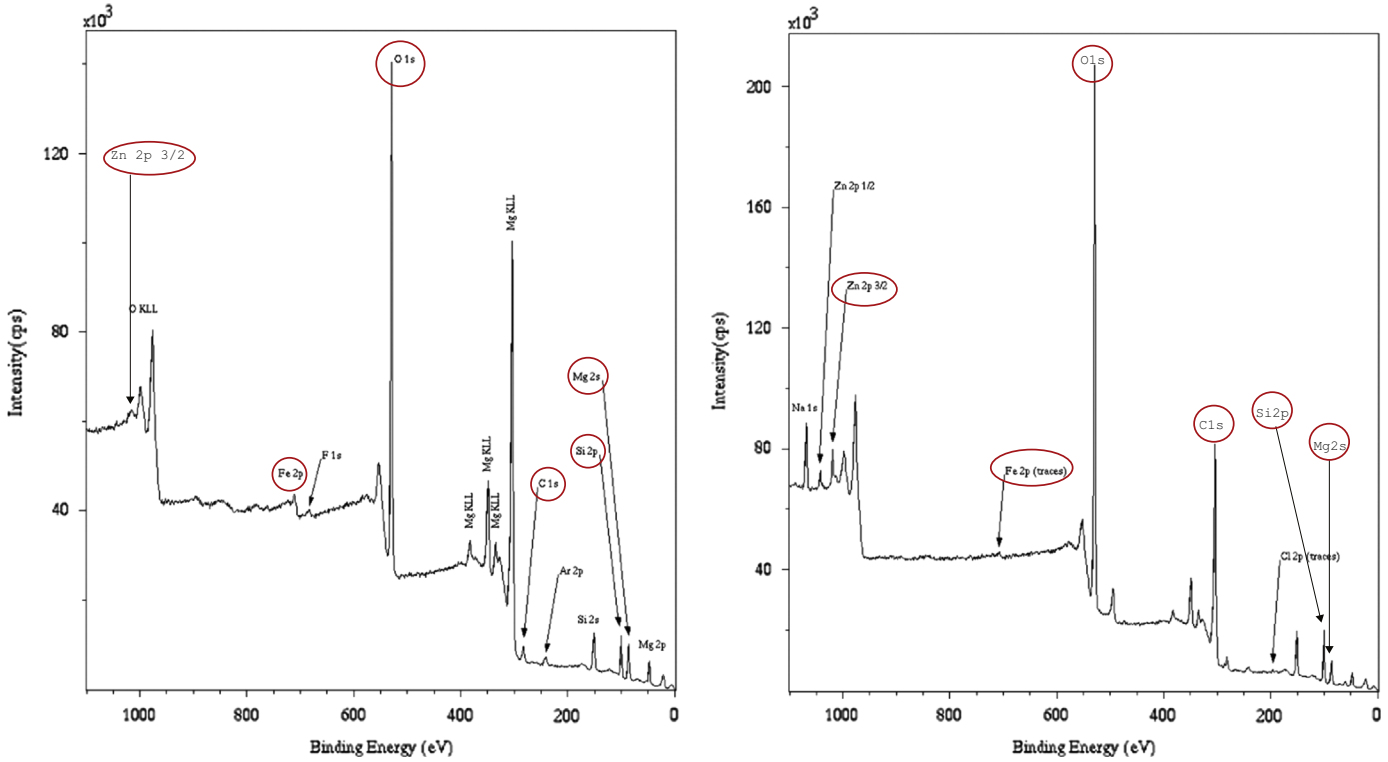

Line	Olivine initial					Olivine reacted 70 C				
	BE, eV	FWHM, eV	AC, at.%			BE, eV	FWHM, eV	AC, at.%		
C 1s	285.0	2.2	5.15	hydrocarbon	C-H, C-C	285.0	1.5	3.3	hydrocarbon	C-H, C-C
	286.9	1.85	0.94	C	C-Cl	286.6	1.6	1.04	C	C-Cl
	289.0	1.85	1.15		COOR	288.7	1.65	0.47		COOR
						290.1	1.4	1.12	carbonate	
O 1s	531.7	2.25	41.42			531.8	1.5	7.14		
	533.1	2.25	18.22			533.1	1.7	51.79		
Si 2p	102.5	2.15	14.49							
						103.9	1.6	19.4		
Mg 2s	88.7	2.2	17			89.9	1.85	12.2		
Fe 2p 3/2	709.8	2.6	1.64				traces			
	712.3	2.9								
Zn 2p 3/2		no				1022.9	1.8	0.45		

Fig. 5. X-ray Photoelectron Spectroscopy Spectrum showing intensity in counts per second (cps) on the *y*-axis and the binding energy in electron volts (eV) on the *x*-axis and a table showing the measured values in Binding energy (BE, eV), Full Width at Half-Maximum (FWHM, eV) and Atomic Concentration (AC, at%). The red rings show measured peaks as presented in the table. (For interpretation of the references to color in this figure legend, the reader is referred to the web version of this article.)

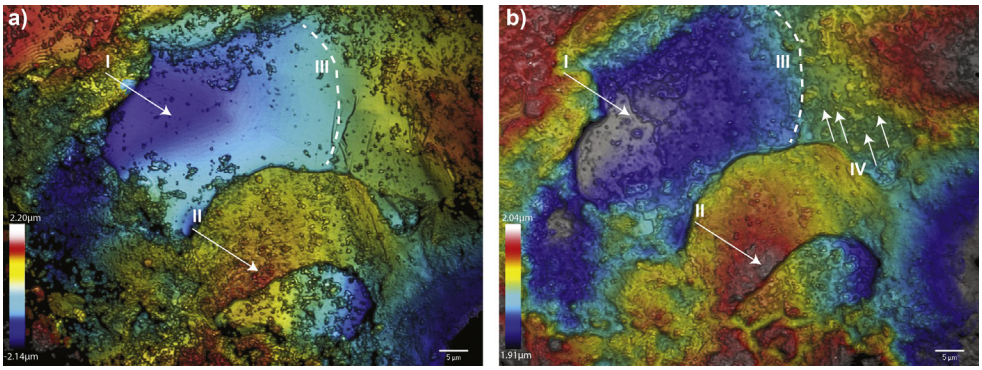

Fig. 6. Profilometry images showing an olivine surface before and after incubation at room temperature for 360 days in which I shows a plain olivine surface that after incubation show an increase roughness and a buildup of amorphous silica, II shows an increased elevation, III shows how a rough area expands into the plain surface and IV shows precipitates of rounded crystals on the surface. Note the different scales.

incorporates both Fe(II) and Fe(III) in its crystal structure and suggest that the formula for ferric talc would be $(Mg_{3-(z+y)}Fe_z^{2+}Fe_y^{3+})(Si_{4-x}Fe_x^{3+})O_{10+y-x}(OH)_{2-y+x}$, which shows that Fe (III) is substituting not only Mg, but also Si. The formula given below is a suggestion of a possible pathway for the oxidation and incorporation of Fe(III) into talc.

$$2(Fe(II),Mg)_2SiO_4 + 2H_2O + SiO_2 = (Mg,Fe_2(II),Fe(III))(Si_3Fe(III))O_{10}(OH)_2 + H_2$$
$$\text{olivine} + \text{water} + \text{silica} \rightarrow \text{talc} + \text{dihydrogen gas} \quad (3)$$

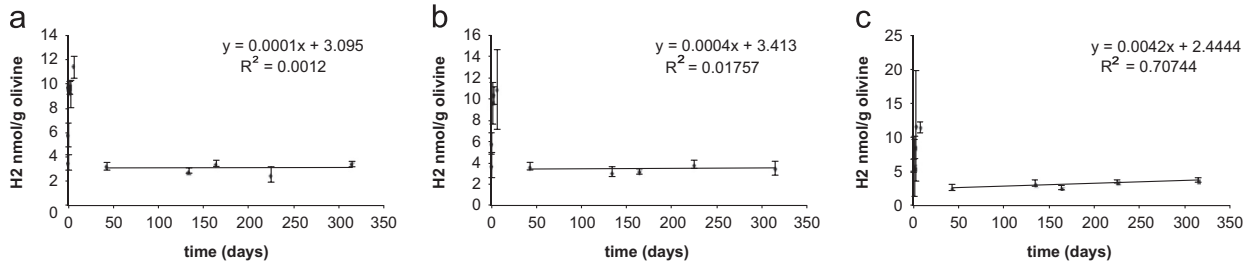

Fig. 7. Concentration of measured headspace H_2 gas plotted as nmol/g olivine at (a) 30 °C, (b) 50 °C and (c) 70 °C from day 43 to day 315. The points represent a mean of three to five replicate samples. The trendline represent the days 43 to 315 only.

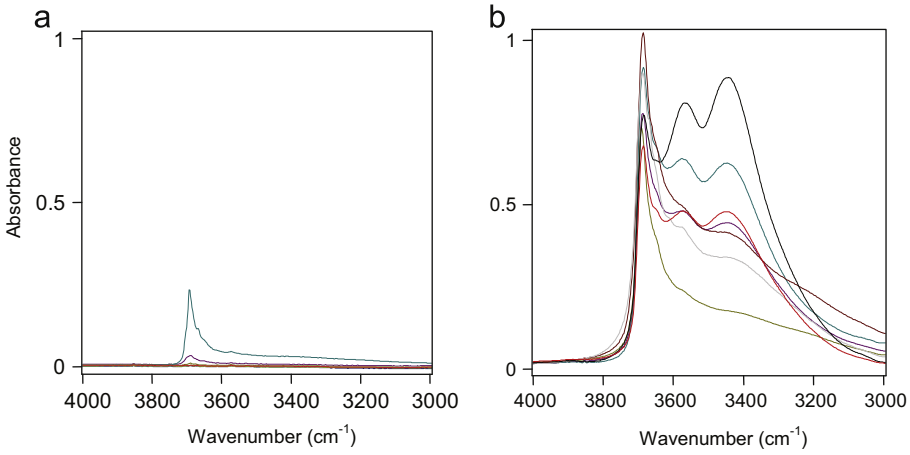

Fig. 8. OH stretching region in the infrared spectra of the olivine thin section with a thickness of 0.2 mm. The spectra were measured at 100 μm × 100 μm areas at 7–7 different, randomly selected places (shown as different colored lines in the spectrum) on (a) the pure olivine crystals, and (b) within the accessory minerals.

Without H_2 being resupplied from serpentinization, H_2 produced earlier in experiments is removed through a variety of processes. For example, H_2 may react with a carbon source to produce CH_4; however, CH_4 formation is a slow process and this does not serve as a major or fast route of H_2 depletion. The slow rate and minimal formation of CH_4 agree with what is observed in our experiments. The most likely scenario is that H_2 continues to work as a buffer removing possible minor quantities of O_2 from the system. With this in mind, H_2 was more than likely to react with O_2 at the onset of the experiments; however, the rate of H_2 production was greater than consumption by O_2. This means that H_2 production rates shown in Fig. 2 are more than likely minimum rates (i.e., faster if no O_2 was present in the system). The non-increasing trend of H_2 accumulation at 30 and 50 °C could also be due to absence of H_2 formation or a formation process too slow to accumulate enough H_2 to create an increase in the background level that was established through the autoclaving process. When olivine sand is autoclaved together with the solution in 120°C for 1 h and at elevated pressures, there is a rapid start of the olivine alteration process and thus also the formation of H_2.

As shown in all of our experiments (Neubeck et al., 2011), H_2 initially increases at the onset of the experiments and then rapidly decreases to near constant after 10 days. This pattern of H_2 evolution may be explained by evaluating the role and dynamics of carbonate formation and H_2 consumption. Initially, carbonates such as calcite are slightly supersaturated in the solutions and carbonate formation is slow at these low temperatures (Palandri and Kharaka, 2004). Both conditions allow Fe^{2+} oxidation related to serpentinization to occur, thereby producing H_2. However, as serpentinization and H_2 production proceed, pH of fluids increases as a result of this process, thereby increasing/forcing carbonate supersaturation as shown in Fig. 9. Over time, the thermodynamic drive for carbonate formation increases. With carbonate formation

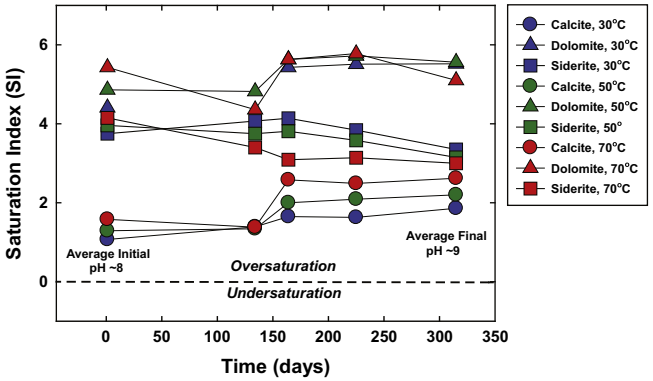

Fig. 9. Calcite and siderite saturation index (SI) values for the abiotic serpentinization experiments at 30, 50 and 70 °C with respect to time (days) are shown.

significantly enhanced, Fe^{2+} oxidation would be suppressed as carbonate formation is a faster process as shown by Jones et al. (2010). At this point (i.e., at ~10 days), H_2 production is limited.

3.4. PHREEQC modeling

All the PHREEQC modeling results represent equilibrium conditions, whereas the experiment system is clearly a non-equilibrium system. All modeling results are made with the purpose of understanding especially the formation of solid products. The kinetic factors that play an important role in experiments are in the model prediction based on an idealized, equilibrium system.

Modeled results of elemental release into solution follow a general trend; however, a large spread is present in the first 43 days of experiment of incubation (Fig. 10) due to autoclaving and

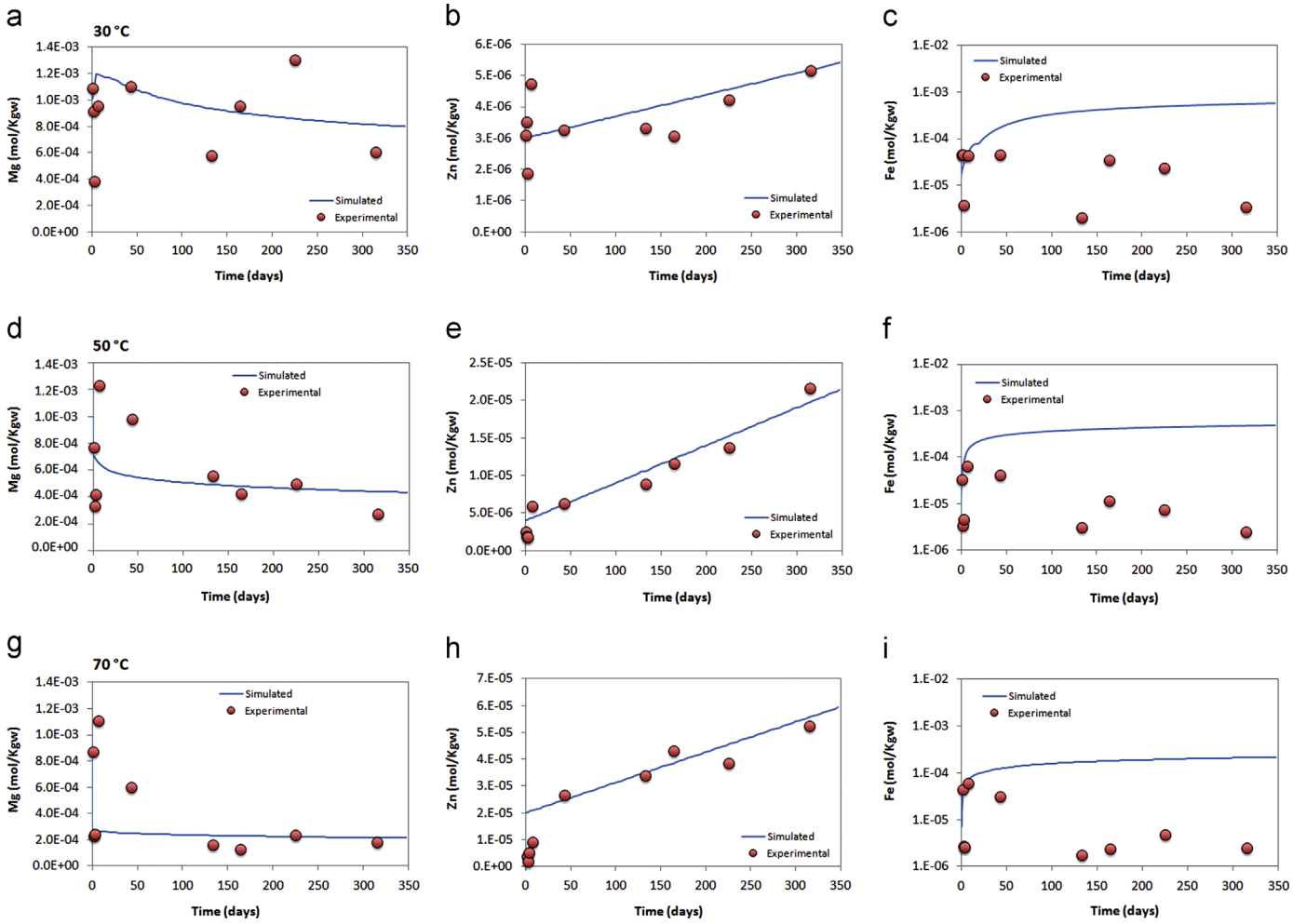

Fig. 10. ICP-AES and PHREEQ-C analyses of Mg (a–c), Zn (d–f) and Fe(g–i) in solution in the experiments conducted at 30 (a, d, g), 50 (b, e, h) and 70 °C (c, f, i). Featured plots show the total amount of the element concentration in ppb. No withdrawal of control input was made. Red dots are the measured values and the blue line represents the predicted PHREEQC value. (For interpretation of the references to color in this figure legend, the reader is referred to the web version of this article.)

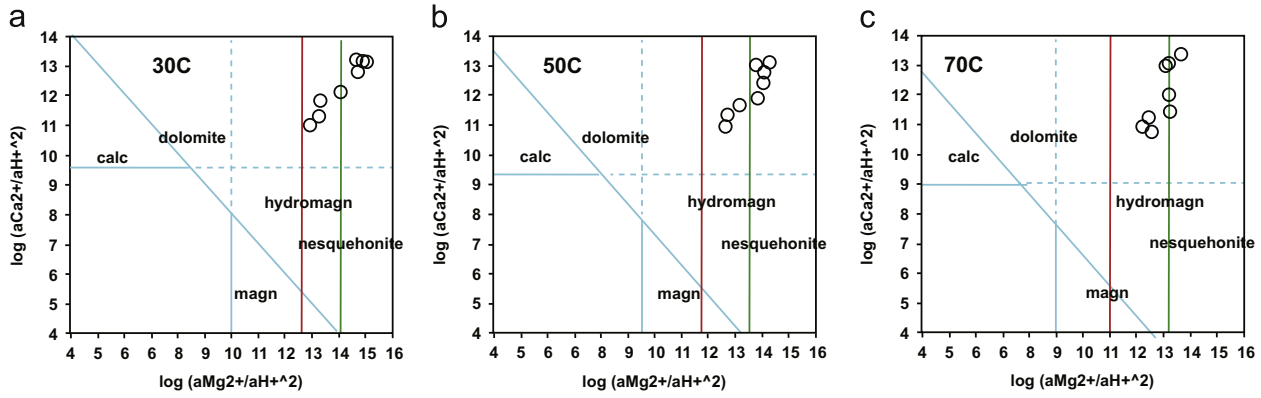

Fig. 11. Aqueous activity diagrams showing the experimental datapoints (circles) compared to the solubilities of calcite ($CaCO_3$), dolomite ($MgCa(CO_3)_2$), magnesite ($MgCO_3$), hydromagnesite ($Mg_5(CO_3)_4(OH)_2 \cdot 4H_2O$) and nesquehonite ($MgCO_3 \cdot 3H_2O$). Dashed lines denotes metastable regions.

thus an increased reaction rate in the experiment bottles, generating a rapid release of elements into the system. After 43 days of incubation and taking error into consideration (Fig. 10 d, e, and g, h) it can be concluded that there is a low spread and high conformity of Mg and Zn data points, signifying an actual fluctuation. The Zn results show a linear increase with time and no sign of reaching equilibrium. Modeled and measured values for Fe in solution are conflicting (10 c,f,i). The modeled Fe concentrations increase with time and reach a steady-state after 50–60 days of incubation, whereas the actual concentrations decrease. The model predicts a steady-state saturation of Fe at about 10^{-4} mol/kgw, whereas the experiment results show that an almost steady state is reached at 10^{-6} mol/kgw. The lower agreement between modeled and measured Fe values is likely due to the lack of possible intermediate secondary precipitates in the PHREEQ-C database. The actual precipitation rate will thus be higher and

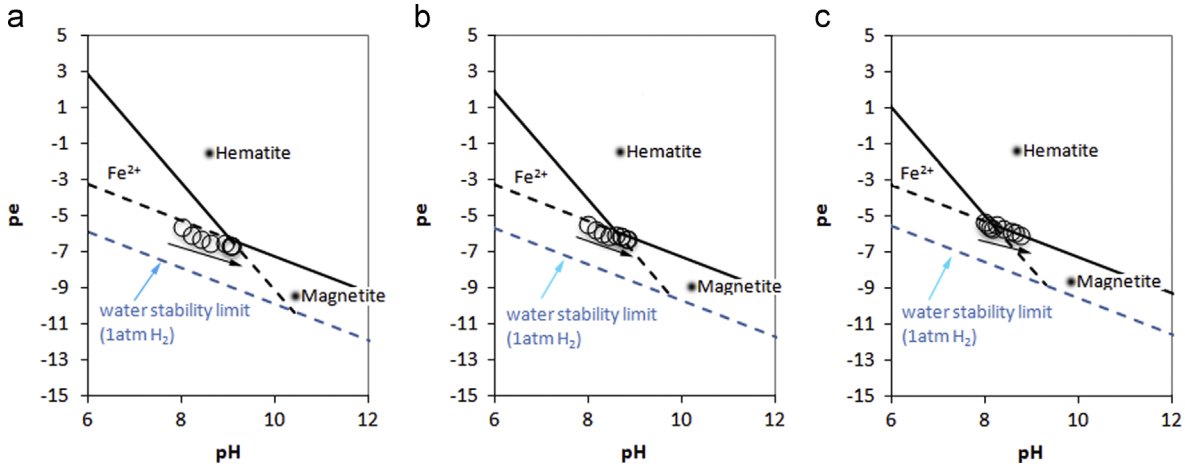

Fig. 12. Experimental datapoints (circles) compared to the stability fields of hematite, magnetite, and Fe^{2+} at total Fe of 10^{-8} mol/Kgw. The dashed black lines denote metastable divides, whereas the blue dashed lines give the water stability at 1 atm H_2. The black arrows indicate the direction in which experimental solutions evolved. (a) 30 °C, (b) 50 °C and (c) 70 °C. (For interpretation of the references to color in this figure legend, the reader is referred to the web version of this article.)

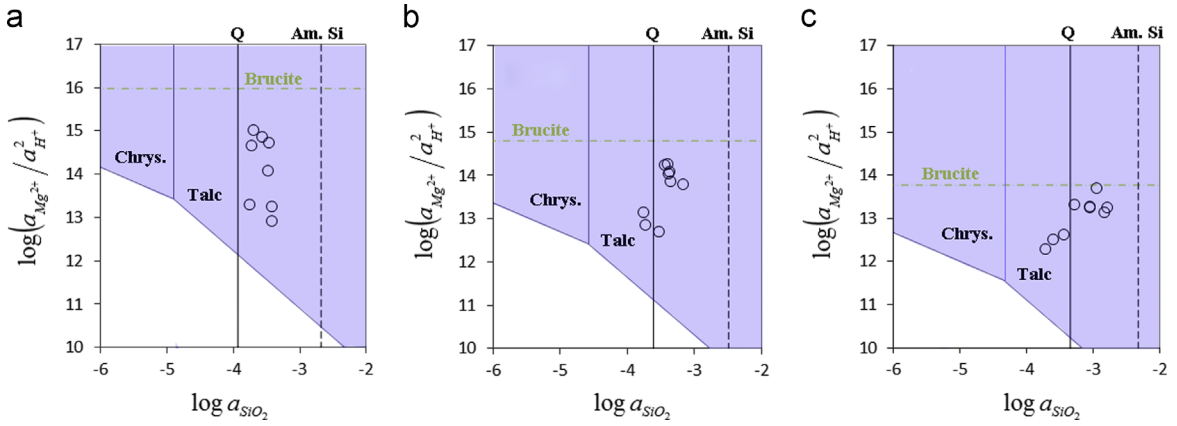

Fig. 13. Aqueous activity diagrams for MgO–SiO_2–H_2O system (a–c). Circles shows the experimental datapoints and the arrows indicate the overall direction of the aqueous solutions with time. (a) 30 °C, (b) 50 °C and (c) 70 °C.

faster than the modeled predictions. In general, there is an increased agreement for Mg and Zn data between the modeled and the actual results with increased temperatures. A better agreement with the modeled and actual results are likely due to the fact that the experiment system is closer to equilibrium at higher temperatures.

Due to the presence of carbonates observed in the experiments by ESEM, XPS (Figs. 3 and 5, respectively) and IR (Fig. 4) and the ambiguous mineralogical data, the stability of carbonates was investigated through PHREEQC modeling using measured Mg and Ca data and pH (Fig. 11). The $(Mg^{2+})/(H^+)^2$ ratio appears to increase and pass both pure magnesite ($MgCO_3$) and hydromagnesite ($Mg_5(CO_3)_4(OH)_2 \cdot 4H_2O$) before approaching the saturation value of nesquehonite ($MgCO_3 \cdot 3H_2O$). Experimental solutions are suggested to be undersaturated with respect to pure iron oxides at 30 °C and for most of the 50 °C samples. The olivine alteration leads to progressively more reducing conditions and higher pH and experiments, therefore, all progress towards the magnetite stability field. At 70 °C, most solutions are close to or within the magnetite stability field and the reactions appear to progress along the hematite–magnetite univariant divide (Fig. 12). The aqueous solutions are within the talc stability field (Fig. 13) approaching brucite and amorphous silica.

The dynamics of carbonate saturation over time are assessed in Fig. 9 where calcite ($CaCO_3$), siderite ($FeCO_3$) and dolomite ($CaMg(CO_3)_2$) saturation index (SI) values are shown. These SI values were calculated using average pH, Ca, Mg, Fe (as Fe^{2+} due to the basic pHs and reducing conditions), and HCO_3^- values obtained from direct measurements of the fluids. Note that not all experimental runs are included in Fig. 9 due to insufficient data to perform the calculation. Sodium was excluded to simplify the calculations. By assuming Fe as Fe^{2+}, siderite SI values reported are maximum values and will be less if Fe redox speciation was allowed to occur. At the onset of the experiment, pH values are ~8; however, these values increase rapidly within the first 10 days arriving at average final pH values for the experiments of ~9. All experiments are supersaturated with respect to calcite, siderite and dolomite. Siderite and dolomite are more supersaturated with respect to calcite. Calcite is more saturated at higher temperatures and vice versa for siderite. More importantly, calcite (and to some extent dolomite) supersaturation increases with respect to time, whereas siderite supersaturation decreases (i.e., approaches equilibrium).

3.5. Carbonates and Si

Due to the low crystallinity of the precipitated material (observed using optical microscopy), some techniques failed to establish statistically reliable spectra for mineral determination. Minerals such as siderite were detected only once by Raman and have to be considered with caution. However, all techniques (ESEM, Raman, IR and XPS) confirm the presence of carbonate phases. Model predictions suggest a supersaturated solution with respect to $CaCO_3$ (Fig. 11) at all

temperatures and an increased stability with increasing temperature with respect to nesquehonite. At 30 °C, the stability field is extended over the stability of hydromagnesite and nesquehonite, which is in agreement with similar studies under the same conditions (Hänchen et al., 2008). Magnesite ($MgCO_3$) is reported to require temperatures over 60 °C, elevated CO_2 pressures and/or high salinities to precipitate but nesquehonite, on the other hand, is reported to occur at 25 °C and pCO_2= 1 bar (Zhang et al., 2006). At higher temperatures, nesquehonite is usually transformed into hydromagnesite, which is in contrast to experiments studied here. The explanation for this partial dehydration-process when transforming highly hydrated hydromagnesite into nesquehonite is likely due to slow kinetics and a non-equilibrium system. The addition of Si to a solution supersaturated with respect to carbonate enhances and stabilizes the amorphicity of the precipitated carbonates through co-precipitation (Kellermeier et al., 2010). This would explain why much of the precipitated material is not entirely crystalline and why Si is not increasing linearly (Fig. 1j–o). Utilizing Zn as a tracer for olivine dissolution, it is clear that the olivine dissolution is not negatively affected by precipitation (Fig. 1 a–c), due to C and Si-rich layer only covering some parts of the olivine surface (Fig. 6). In summary, carbonates were co-precipitating with Si, preventing magnesite to precipitate and causing the system to, according to the predicted PHREEQ-C modeled results, reside within the stability field of hydromagnesite and nesquehonite.

4. Conclusions

Our results show that H_2 forms through the alteration of natural olivine and accessory minerals at temperature as low as 30 °C without the precipitation of magnetite. The formation rate of H_2 as well as the precipitation rate of secondary minerals was highest at 70 °C. The main difference between experiments at different temperatures are reaction rates, which cause olivine to alter faster and H_2 to form faster at 70 °C compared with 50 °C and 30 °C. We suggest that the electron acceptor for the oxidation of aqueous Fe(II) is the precipitation of intermediate talc/serpentine-resembling species (according to Eq. (3)) observed by Raman, IR, ESEM and XPS. This is also supported by PHREEQC modeling that suggests that the aqueous solutions are within the stability field of talc. A major part of Fe(III) was found in precipitates in solution and not on the olivine surface, suggesting that a major part of ferrous oxidation was coupled to the metastable, intermediate and amorphous phases of talc and a minor part coupled to the formation of serpentine minerals on the olivine surfaces. Previous studies have shown that spinels may act as strong catalysts for H_2 formation at low temperatures (Mayhew et al., 2013), which is in agreement with this study because of the presence of spinel phases within the initial bulk material (Neubeck et al., 2011).

The results from these experiments and modeling also support a similar redox reaction pathway for iron as reported by Jones et al. (2010) in which there is preferential incorporation of Fe(II) in carbonates rather than an oxidation of Fe(II) when the alteration of olivine occurs in a carbonate-supersaturated solution. This simple and evidence-supported pathway explains the lack of H_2 increase in these experiments and may explain low H_2 and H_2-driven CH_4 production levels observed in other experiments. A buildup of an uneven Si-rich layer was observed on the olivine surface allowing for further olivine dissolution. This allows the serpentinization reaction to proceed even though precipitation is occurring both on the surface of the olivine and in the solution.

Kral et al. (1998) show that some microorganisms can be sustained in H_2 concentrations as low as 13 ppm which is in the range of the average concentration in this study in which an average of ~15 ppm was accumulated in the experiments carried out at 30 °C after 315 days of incubation. Therefore, enough H_2 could form from natural low temperature serpentinization environments to sustain certain microbial communities (Kral et al., 1998; Schnürer et al., 1997) even when the system is carbonate supersaturated. Our study implies that low temperature and far from equilibrium serpentine environments (e.g., such as the peridotite outcrops in the Ronda massif in Spain (Gervilla and Leblanc, 1990; van der Wal and Vissers, 1996) or other continental serpentine outcrops with low temperatures) could be plausible for hydrogenotrophic life. Another environment that could meet the criteria of sustaining hydrogenotrophic life at depths could be the deep Martian subsurface, where liquid water is probable and where all essential elements are present.

Acknowledgments

This work has been supported by the Swedish Research Council (Contract no. 621-2008-2712) and the Astrobiology graduate school. We want to acknowledge the help and support from Andrei Schukarev at Umeå University, Erik Jonsson at SGU, Marianne Ahlbom, Curt Broman and José Godinho at Stockholm University, Christian Mille from YKI and Kjell Jansson and Jekabs Grins from the Department of Materials Science, Stockholm University. We also wish to acknowledge Professor Norman Sleep and an anonymous reviewer for valuable comments.

Appendix A. Supporting information

Supplementary data associated with this article can be found in the online version at http://dx.doi.org/10.1016/j.pss.2014.02.014.

References

Berndt, M.E., Allen, D.E., Seyfried, W.E., 1996. Reduction of CO_2 during serpentinization of olivine at 300 °C and 500 bar. Geology 24, 351–354.
Charlou, J.L., Donval, J.P., Fouquet, Y., Jean-Baptiste, P., Holm, N.G., 2002. Geochemistry of high H_2 and CH_4 vent fluids issuing from ultramafic rocks at the Rainbow hydrothermal field (36°14′ N, MAR). Chem. Geol. 191, 1428–1434.
Evans, B.W., 2008. Control of the products of serpentinization by the $Fe^{2+}Mg^{-1}$ exchange potential of olivine and orthopyroxene. J. Petrol. 49, 1873–1887.
Evans, B.W., 2010. Lizardite versus antigorite serpentinite: magnetite, hydrogen and life(?) Geology 38, 879–882.
Forbes, W.C., 1971. Iron content of talc in the system $Mg_3Si_4O_{10}(OH)_2$–$Fe_3Si_4O_{10}(OH)_{12}$. J. Geol. 79, 63–74.
Forbes, W.C., 1969. Unit-cell parameters and optical properties of talc on the join $Mg_3Si_4O_{10}(OH)_2$–$Fe_3Si_4O_{10}(OH)_2$. Am. Mineral. 54, 1399–1408.
Frost, B.R., 1985. On the stability of sulfides, oxides, and native metals in serpentinite. J. Petrol. 26, 31–63.
Frost, B.R., Beard, J.S., 2007. On silica activity and serpentinization. J. Petrol. 48, 1351–1368.
Früh-Green, G.L., Connolly, J.A., Plas, A., Kelley, D.S., Grobéty, B., 2004. Serpentinization of oceanic peridotites: implications for geochemical cycles and biological activity. In: The Subseafloor Biosphere at Mid-Ocean Ridges, Geophysical Monograph Series, 144. American Geophysical Union, pp. 119–136.
Gervilla, F., Leblanc, M., 1990. Magmatic ores in high-temperature alpine-type lherzolite massifs (Ronda, Spain, and Beni Bousera, Morocco). Econ. Geol. 85, 112–132.
Giammar, D.E., Bruant Jr., R.G., Peters, C.A., 2005. Forsterite dissolution and magnesite precipitation at conditions relevant for deep saline aquifer storage and sequestration of carbon dioxide. Chem. Geol. 217, 257–276.
Golightly, P.J., Arancibia, O.N., 1979. The chemical composition and infrared spectrum of nickel- and iron-substituted serpentine from a nickeliferous laterite profile, Soroako, Indonesia. Can. Mineral. 17, 719–728.
Golubev, S.V., Pokrovsky, O.S., Schott, J., 2005. Experimental determination of the effect of dissolved CO_2 on the dissolution kinetics of Mg and Ca silicates at 25 °C. Chem. Geol. 217, 227–238.
Haggerty, J., 1991. Evidence from fluid seeps atop serpentine seamounts in the Mariana forearc: clues for emplacement of the seamounts and their relationship to forearc tectonics. Mar. Geol. 102, 293–309.
Haug, T.A., Kleiv, R.A., Munz, I.A., 2010. Investigating dissolution of mechanically activated olivine for carbonation purposes. Appl. Geochem. 25, 1547–1563.
Hänchen, M., Prigiobbe, V., Baciocchi, R., Mazzotti, M., 2008. Precipitation in the Mg-carbonate system—effects of temperature and CO_2 pressure. Chem. Eng. Sci. 63, 1012–1028.

Hänchen, M., Prigiobbe, V., Storti, G., Seward, T.M., Mazzotti, M., 2006. Dissolution kinetics of fosteritic olivine at 90–150 °C including effects of the presence of CO_2. Geochim. Cosmochim. Acta 70, 4403–4416.
Hellevang, H., 2008. On the forcing mechanism for the H_2-driven deep biosphere. Int. J. Astrobiol. 7, 157–167.
Hietanen, A.M., 1973. Geology of the Pulga and Bucks Lake Quadrangles
Holm, N.G., Charlou, J.L., 2001. Initial indications of abiotic formation of hydrocarbons in the Rainbow ultramafic hydrothermal system, Mid-Atlantic Ridge. Earth Planet. Sci. Lett. 191, 1–8.
Hugoni, M., Taib, N., Debroas, D., Domaizon, I., Dufournel, I.J., Bronner, G., Salter, I., Agogué, H., Mary, I., Galand, P.E., 2013. Structure of the rare archaeal biosphere and seasonal dynamics of active ecotypes in surface coastal waters. Proc. Natl. Acad. Sci. USA 110, 6004–6009.
Jones, L.C., Rosenbauer, R., Goldsmith, J.I., Oze, C., 2010. Carbonate control of H_2 and CH_4 production in serpentinization systems at elevated P-Ts. Geophys. Res. Lett. 37, L14306.
Kellermeier, M., Melero-Garcia, E., Glaab, F., Klein, R., Drechsler, M., Rachel, R., Garcia-Ruiz, J.M., Kunz, W., 2010. Stabilization of amorphous calcium carbonate in inorganic silica-rich environments. J. Am. Chem. Soc. 132, 17859–17866.
Khallaf, H., Chai, G., Lupan, O., Heinrich, H., Park, S., Schulte, A., Chow, L., 2009. Investigation of chemical bath deposition of ZnO thin films using six different complexing agents. J. Phys. D 42, 135304.
Klein, F., Bach, W., McCollom, T.M., 2013. Compositional controls on hydrogen generation during serpentinization of ultramafic rocks. Lithos 178, 55–69.
Konn, C., Holm, N.G., Donval, J.P., Charlou, J.L., 2009. Organic compounds in hydrothermal fluids from ultramafic-hosted vents of the Mid Atlantic Ridge: an update on composition and origin. Geochim. Cosmochim. Acta 73, A679.
Kral, T.A., Brink, K.M., Miller, S.L., McKay, C.P., 1998. Hydrogen consumption by methanogens on the early Earth. Orig. Life Evol. Biosph. 28, 311–319.
Krumholz, L.R., 2000. Microbial communities in the deep subsurface. Hydrogeol. J. 8, 161–176.
Marcaillou, C., Munos, M., Vidal, O., Parra, T., Harfouche, M., 2011. Mineralogical evidence for H_2 degassing during serpentinization at 300 C/300 bar. Earth Planet. Sci. Lett. 303, 281–290.
Mayhew, L.E., Ellison, E.T., McCollom, T.M., Trainor, T.P., Templeton, A.S., 2013. Hydrogen generation from low-temperature water–rock reactions. Nat. Geosci. 6, 478–484.
McCollom, T.M., Bach, W., 2009. Thermodynamic constraints on hydrogen generation during serpentinization of ultramafic rocks. Geochim. Cosmochim. Acta 73, 856–875.
McDonough, W.F., Sun, S.S., 1995. The composition of the Earth. Chem. Geol. 120, 223–253.
Nealson, K.H., Inagaki, F., Takai, K., 2005. Hydrogen-driven subsurface lithoautotrophic microbial ecosystems (SLiMEs): do they exist and why should we care? Trends Microbiol. 13, 405–410.
Neubeck, A., Duc, N.T., Bastviken, D., Crill, P., Holm, N.G., 2011. Formation of H_2 and CH_4 by weathering of olivine at temperatures between 30 and 70 °C. Geochem. Trans. 12, 6.
Noack, Y., Decarreau, A., Manceau, A., 1986. Spectroscopic and oxygen isotopic evidence for low and high temperature origin of talc. Bull. Minéral. 109, 253–263.
Oelkers, E.H., Schott, J., Gauthier, J-M., Herrero-Roncal, T., 2008. An experimental study of the dissolution mechanism and rates of muscovite. Geochim. Cosmochim. Acta 72, 4948–4961.
Oze, C., Jones, L.C., Goldsmith, J.I., Rosenbauer, R.J., 2012. Differentiating biotic from abiotic methane genesis in hydrothermally active planetary surfaces. Proc. Natl. Acad. Sci. USA 109, 9750–9754.
Palandri, J.L., Kharaka, Y.K., 2004. A Compilation of Rate Parameters of Water-Mineral Interaction Kinetics for Application to Geochemical Modeling: US Geological Survey Water-Resources Investigations Report 04-1068.
Parkhurst, D.L., Appleo, C.A., 1999. Users guide to PHREEQC (version 2)—a computer program for speciation, batch reaction, one dimensional transport, and inverse geochemical calculation. US Geological Survey (Water-Resources Investigations Reports)
Pedersen, K., 1993. The deep subterranean biosphere. Earth-Sci. Rev. 34, 243–260.
Pokrovsky, O.S., Schott, J., 2000a. Kinetics and mechanism of forsterite dissolution at 25 °C and pH from 1 to 12. Geochim. Cosmochim. Acta 64, 3313–3325.
Pokrovsky, O.S., Schott, J., 2000b. Forsterite surface composition in aqueous solutions: a combined potentiometric, electrokinetic, and spectroscopic approach. Geochim. Cosmochim. Acta 64, 3299–3312.
Prigiobbe, V., H nchen, M., Costa, G., Baciocchi, R., Mazzotti, M., 2009. Analysis of the effect of temperature, pH, CO_2 pressure and salinity on the olivine dissolution kinetics. Energy Procedia 1, 4881–4884.
Schnürer, A., Svensson, B.H., Schink, B., 1997. Enzyme activities in and energetics of acetate metabolism by the mesophilic syntrophically acetate-oxidizing anaerobe Clostridium ultunense. FEMS Microbiol. Lett. 154, 331–336.
Schulte, M., Blake, D., Hoehler, T., McCollom, T.M., 2006. Serpentinization and its implications for life on the early Earth and Mars. Astrobiology 6, 364–376.
Schulze, R.K., Hill, M.A., Field, R.D., Papin, P.A., Hanrahan, R.J., Byler, D.D., 2004. Characterization of carbonated serpentine using XPS and TEM. Energy Convers. Manag. 45, 3169–3179.
Schwarzenbach, E.M., Früh-Green, G.L., Bernasconi, S.M., 2013. Serpentinization and carbon sequestration: a study of two ancient peridotite-hosted hydrothermal systems. Chem. Geol. 351, 115.
Seyfried Jr., W.E., Foustoukos, D.I., Fu, Q., 2007. Redox evolution and mass transfer during serpentinization: an experimental and theoretical study at 200 °C, 500 bar with implications for ultramafic-hosted hydrothermal systems at Mid-Ocean Ridges. Geochim. Cosmochim. Acta 71, 3872–3886.
Sleep, N.H., Bird, D.K., Pope, E.C., 2011. Serpentinite and the dawn of life. Philos. Trans. R. Soc. B: Biol. Sci. 366, 2857–2869.
Sobolev, A.V., Hofmann, A.W., Sobolev, S.V., Nikogosian, I.K., 2005. An olivine-free mantle source of Hawaiian shield basalts. Nature 434, 590–597.
van der Wal, D., Vissers, R., 1996. Structural petrology of the Ronda Peridotite, SW Spain: deformation history. J. Petrol. 37, 23–43.
Wilkins, R.W.T., Ito, J., 1967. Infrared spectra of some synthetic talcs. Am. Mineral. 52, 1649–1661.
Xu, J.F., Ji, W., Lin, J.Y., Tang, S.H., Du, Y.W., 1998. Preparation of ZnS nanoparticles by ultrasonic radiation method. Appl. Phys. A: Mater. Sci. Process. 66, 639–641.
Yariv, S., Heller-Kallai, L., 1975. The relationship between the I.R. spectra of serpentines and their structures. Clays Clay Miner. 23, 145–152.
Zhang, Z., Zheng, Y., Ni, Y., Liu, Z., Chen, J., Liang, X., 2006. Temperature- and pH-dependent morphology and FT-IR analysis of magnesium carbonate hydrates. J. Phys. Chem. B 110, 12969–12973.